CEAS
Council of European Aerospace Societies

Large Eddy Simulation of Multiport Injector Array Transition

Nicholas N. Gibbons[1]*, Tristan Vanyai*[1]*, Vincent Wheatley*[1]

Abstract

A numerical study of compressible turbulent transition behind a multiport injector array (MPIA) is conducted. The flow domain corresponds to an axisymmetric inlet recently tested at The University of Queensland that used an MPIA to trip the boundary layer, by injecting a small amount of nitrogen close to the wall. A single row of four 0.2mm porthole injectors is simulated using Wall-Modelled Large Eddy Simulation (LES), at an experimental condition corresponding to Mach 7.6 flight at a dynamic pressure of 50kPa. The LES simulations reveal that the MPIA injection results in immediate large scale instabilities reminiscent of near-wall turbulence. The main feature of interest is a family of dominant frequencies superimposed on the turbulent wavestructure, with a base wavelength of $\approx 5mm$. The source of this regularity appears to be periodic oscillation of the final fuel jet, which in turn is dynamically coupled to the upstream jets in an complex and interesting manner which has not been described before. The turbulent flow behind the MPIA results in an increase in wall heat transfer that counteracts any film cooling that may be present from the injectors. The LES prediction of the heat transfer rates compare favourably to experimental measurements, and RANS simulations using the Spalart-Allmaras and Menter SST models are found to underpredict wall heat transfer throughout the domain.

Keywords: *Large Eddy Simulation, Hypersonics, Transition*

Nomenclature

$\dot{\omega}_s$	Chemical reaction rate of species s (kg/m^3/s)	p	Pressure (Pa)
$\hat{\nu}$	Spalart-Allmaras working variable	q_j	Thermal Conduction Vector (J/m^2/s)
ν_t	Kinematic Turbulent Viscosity (m^2/s)	t_{ji}	Viscous Stress Tensor (kg/m^2/s^2)
ρ_s	Partial density of species s (kg/m^3)	u_j	jth component of the velocity vector (m/s)
E	Energy Density (J/m^3)	v_{sj}	Diffusion flux tensor of species s in the j direction (kg/m^2/s)

1. Introduction

Air-breathing hypersonic flight has proven to be a formidable engineering challenge. Among the many problems associated with flying many times faster than the speed is sound is thermal protection — How to prevent the vehicle from melting under the intense heat load delivered by the extreme kinetic energy of the incoming flow. Active cooling of some description will likely be needed to address this problem, but its severity can also be mitigated using film cooling, where a thin layer of cold fuel is injected along an external surface to insulate it from the hot freestream.

The most optimal system for actually delivering this fuel is still a matter of debate. A backward facing step with a slot injector is one solution [1] and another is porous walls made from ceramic or carbon-composite material [2], where the high pressure fuel is forced through the entire structure in a continuous fashion, simultaneously cooling the wall and oozing into the boundary layer. A discrete equivalent to this idea is the Multiport Injector Array (MPIA): A battery of small porthole injectors, each less than a millimetre in diameter, that inject a small amount of fuel into the boundary layer in a more controlled manner than a porous wall.

---

[1]*School of Mechanical and Mining Engineering, University of Queensland, St. Lucia QLD 4072, Australia*

MPIAs are versatile and complicated systems that have a diverse set of applications. These include mixing enhancement, film cooling, drag reduction, and tripping a laminar boundary layer into turbulent state. This diversity is a result of the complex physical interactions occurring in an MPIA flowfield: Transition, turbulent mixing, shock boundary layer interactions, and possibly even combustion if the free stream pressure is high.

The simplest and most common approach to modelling this complexity is to use Reynolds Averaged Navier-Stokes (RANS) based numerical simulations. Examples include [3] (focused on enhancing mixing efficiency), as well as [4] and [5] (focused on film cooling, the former using a flat plate and the latter a blunt cone). In both these cases the MPIAs produced significant film cooling and drag reduction, though the relationship is more complicated when combustion is present, as demonstrated in [6]. Near-wall combustion tends to reduce drag further by lowering the density in the boundary layer, an effect predicted by [7] using an extension of Van Driest boundary layer theory. Less obviously, mild combustion can also decrease the heat transfer, as long as the boundary layer rarefaction effect is stronger than the increase in total temperature from the chemical heat release. Both Stalker and Pudsey document this phenomenon, though the cross over point where more combustion leads to greater heat transfer rather than less is in dispute.

At present much of this work is hypothetical, and experimental studies of MPIAs are few and far between. The best recent experiment to directly study an MPIA is [8], who compared a hydrogen fuel MPIA to two different porous injectors at on a turbulent flat plate at Mach 8 at a dynamic pressure 50 kPa. The study found direct evidence of film cooling from both types of injectors by measuring the wall heat transfer with sensors behind the injectors, with more injectant resulting in more film cooling. The experiments also addressed the use of MPIAs as transition enhancers by removing the physical turbulent trips from the plate and injecting fuel into a laminar boundary layer. Heat transfer levels in this configuration were low directly behind the injection point, but quickly climbed up to the turbulent level over the ≈ 100 mm downstream. The most obvious interpretation of this result is that the injection caused transition, but the mechanics of this process are mostly unknown. Since fluidic trips have advantages over physical trips for some applications, it will be important to understand their physical behaviour before deploying them in flight.

To advance this goal, this paper applies high fidelity Large Eddy Simulation of the MPIAs tested in a new set of experiments, using an axisymmetric model scramjet inlet tested in the T4 shock tunnel at The University of Queensland in 2019. In the experiment the MPIA was used primarily as a turbulent trip, with Nitrogen used as an injectant with similar molecular mass to a light hydrocarbon fuel. Of interest are the mechanics of turbulent transition occurring behind the MPIA, as well as the accuracy of standard numerical turbulence models in predicting wall heat transfer in such a complicated flow field. Vortex visualisation and advanced spectral postprocessing will be used to explore the flow features and discuss the mechanics of transition. The LES results also provide a cutting edge prediction of the wall heat transfer rate behind the injectors, which will be compared to some preliminary experimental data, alongside more traditional Reynolds-Averaged Navier-Stokes (RANS) based simulations.

2. Flow Description

The numerical results in this paper are generated using two simulation domains, an axisymmetric simulation of an inverted cone without injectors representing the model inlet, and a much finer simulation of a single row of injectors in full 3D, corresponding to a 5° sector of the larger domain (see figure 1). The flow from the upstream (larger) grid is fed into the downstream (smaller) one using the flux-preserving boundary condition described in [9], which takes advantage of the directionality of supersonic information propagation to map flow from one grid to another. This allows the Large Eddy Simulation grid to be of very high resolution without having to resolve the entire flow domain up to the leading edge.
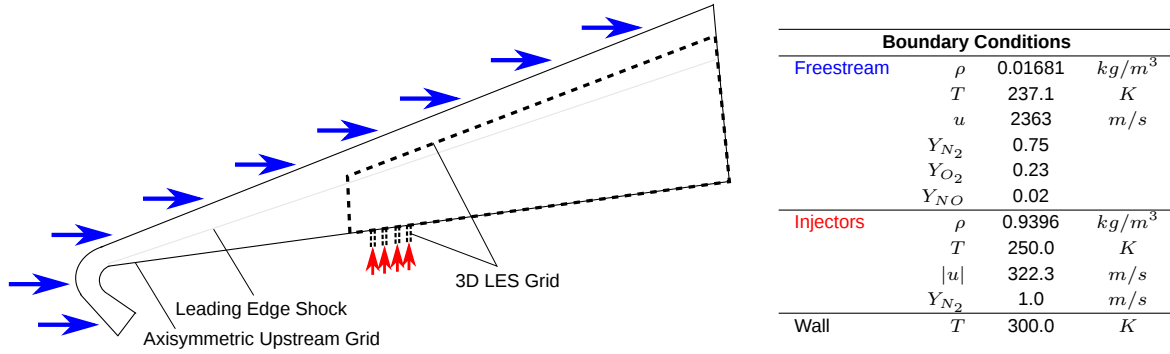

Boundary Conditions			
Freestream	ρ	0.01681	kg/m^3
	T	237.1	K
	u	2363	m/s
	Y_{N_2}	0.75	
	Y_{O_2}	0.23	
	Y_{NO}	0.02	
Injectors	ρ	0.9396	kg/m^3
	T	250.0	K
	$|u|$	322.3	m/s
	Y_{N_2}	1.0	m/s
Wall	T	300.0	K

Fig 1. Gridding strategy and boundary conditions schematic

3. Numerical Method

Fluid flow in these domains is simulated using Unstructured 3D (US3D), a hybrid structured/unstructured compressible flow solver for aerospace applications developed at The University of Minnesota ([10]). US3D solves the set of compressible gas transport equations for the mass of each chemical species, momentum in each space direction, and overall energy, supplemented with the Improved Delayed Detached Eddy Simulation (IDDES) turbulence model [11]. The transport equation for this model (equation 4) is identical to the compressible Spalart Allmaras RANS model presented in [12], though the DES formulation adds a much more complex function to the lengthscale parameter d, allowing IDDES to operate as a hybrid that computes RANS style turbulence modelling near walls and low dissipation LES elsewhere:

$$\frac{\partial \rho_s}{\partial t} + \frac{\partial}{\partial x_j}(\rho_s u_j) + \frac{\partial}{\partial x_j}(v_{sj}) = \dot{\omega}_s \tag{1}$$

$$\frac{\partial}{\partial t}(\rho u_i) + \frac{\partial}{\partial x_j}(\rho u_j u_i) = -\frac{\partial p}{\partial x_i} + \frac{\partial t_{ji}}{\partial x_j} \tag{2}$$

$$\frac{\partial}{\partial t}(E) + \frac{\partial}{\partial x_j}[(E+p)u_j] = \frac{\partial}{\partial x_j}(u_i t_{ij}) - \frac{\partial q_j}{\partial x_j} \tag{3}$$

$$\frac{\partial \rho \hat{\nu}}{\partial t} + \frac{\partial \rho \hat{\nu} \widetilde{u}_j}{\partial x_j} = \rho c_{b1}(1-f_{t2})\hat{S}\hat{\nu} - \rho\left[c_{w1}f_w - \frac{c_{b1}}{\kappa^2}f_{t2}\right]\left(\frac{\hat{\nu}}{d}\right)^2 + \frac{1}{\sigma}\frac{\partial}{\partial x_j}\left(\rho(\nu+\hat{\nu})\frac{\partial \hat{\nu}}{\partial x_j}\right) + \frac{c_{b2}}{\sigma}\rho\frac{\partial \hat{\nu}}{\partial x_i}\frac{\partial \hat{\nu}}{\partial x_i} \tag{4}$$

The equations are solved by first abstracting them into a vector equation:

$$\frac{\partial \mathbf{U}}{\partial t} + \frac{\partial \mathbf{F}_j}{\partial x_j} - \frac{\partial \mathbf{V}_j}{\partial x_j} = \mathbf{W} \tag{5}$$

Where $\mathbf{U}$ represents the conserved variables of mass, momentum, energy, and turbulent viscosity; $\mathbf{F}$ the inviscid fluxes of each in the j direction; $\mathbf{V}$ the viscous fluxes in the j direction; and $\mathbf{W}$ the remaining terms in equations 1 - 4 that do not involve gradients. Discretising these equations into a mesh of small boxes gives a vector equation for the change in conserved quantities in each box in terms of the flow through each face f:

$$\frac{\partial \mathbf{U}}{\partial t} = -\frac{1}{\mathcal{V}} \sum_f [(\mathbf{F}_{fj} - \mathbf{V}_{fj}) n_{fj} S_f] + \mathbf{W} \tag{6}$$

Where n_{fj} is the normal vector of face f, S_f is the surface area of face f, and $\mathcal{V}$ the volume of the grid cell. In this work $\mathbf{F}_{fj}$ is calculated using a low dissipation hybrid scheme described in [13], extended to 6th order spatial accuracy using gradient reconstruction from nearby cells. The low dissipation flux calculator is needed to support high quality numerical turbulence in an LES, though it is augmented with a switch that adds a dissipative term near shockwaves so that it operate in supersonic flow. Here the switching function of [14] is employed, along with the non-symmetric terms from the modified Steger-Warming method described in [15] to implement the dissipation. $\mathbf{V}_{fj}$ is computed using a weighted least-squares approach that estimates the gradients of the primitive variables using a cloud of seven cells for a hexahedral structured grid.

Time marching is performed using the implicit Full-Matrix Point Relaxation (FMPR) method of [16]. This algorithm computes the change in the conserved quantities over a single timestep $\delta \mathbf{U}_i^0$ for each cell i between, using a sequence of subiterations indexed by k:

$$\delta \mathbf{U}_i^k = \left[I + \frac{\Delta t}{\mathcal{V}_i} \sum_f \left[A^+ + B^+ \right]_f S_j - \Delta t C \right]^{-1} \times \left[\Delta \mathbf{U}_i - \frac{\Delta t}{\mathcal{V}_i} \sum_f \left[(A^- - B^-) \delta \mathbf{U}_o^{k-1} \right]_f S_j \right] \tag{7}$$

Where A, B, and C are the inviscid, viscous, and source term Jacobians in matrix form. In this expression, the $+$ superscript indicates a quantity computed on the inside of the cell's face f and the superscript $-$ computed on the outside of the face. Additionally $\delta \mathbf{U}_o$ is the change in conserved quantity of the cell on the other side of face f and $\Delta \mathbf{U}_i$ the change in conserved quantities predicted by the explicit fluxes. Four iterations of this formula are used to compute each time, with $\delta \mathbf{U}_i^0$ computed by assuming it is equal to $\Delta \mathbf{U}_i$. The time marching is made second order accurate by averaging the RHS term with that of the previous timestep, effectively forming a second order Backward Euler scheme:

$$\Delta \mathbf{U}_i = \frac{1}{2} \left(\Delta \mathbf{U}_i^n + \Delta \mathbf{U}_i^{n-1} \right) \tag{8}$$

The transport properties in these expressions are generated by empirical curve-fits computed by NASA CEA [17] for the viscosity of individual species at a given temperature, combined using the mixing rule of [18] to get the mixture viscosity:

$$\mu = \sum_s \frac{\mu_s X_s}{\phi_s} \quad \phi_s = \sum_m \frac{X_m \left(1 + \sqrt{\mu_s/\mu_m \sqrt{M_m/M_s}} \right)^2}{\sqrt{8(1 + M_s/M_m)}} \tag{9}$$

The heat conduction vector is modelled using Fourier's law, with the laminar thermal conductivity assembled again using the Wilke mixing rule, and the turbulent component derived from a constant turbulent

Prandtl number (Pr_t) of 0.91:

$$q_j = -\kappa \frac{\partial T}{\partial x_j} \quad \kappa = \sum_s \frac{\mu_s X_s}{\phi_s}(c_{v_s} + 2.25 R_s) + \frac{\mu_t}{Pr_t} \tag{10}$$

4. Flowfield Description

A section of the flowfield generated by slicing through the injector symmetry plane is shown in figures 2 - 4. In each image the axes grid has been rotated to align with the wall-normal and wall-parallel directions, hence the designation X' and Y'.

Figure 2 shows the Nitrogen mass fraction Y_{N2}, in this case the injectant that is used as an inert substitute for fuel. The most notable feature of all the flow visualisations is the visible unsteadiness of the fuel plumes, which seem to be transitioning immediately into a state of disordered turbulent-like motion. Away from the immediate vicinity of the injectors the mass fraction drops rapidly, as the nitrogen mixes with the air sweeping in from either side of the plumes. Also quite striking are the series of ring-like structures visible from $X' = 0.11$ to $X' = 0.15$, which suggest that the flow is not immediately entering a fully developed turbulent state but may be passing through a transitional phase with some large scale regularity, similar to the flow results observed by [19] in their study of supersonic cylindrical trips.
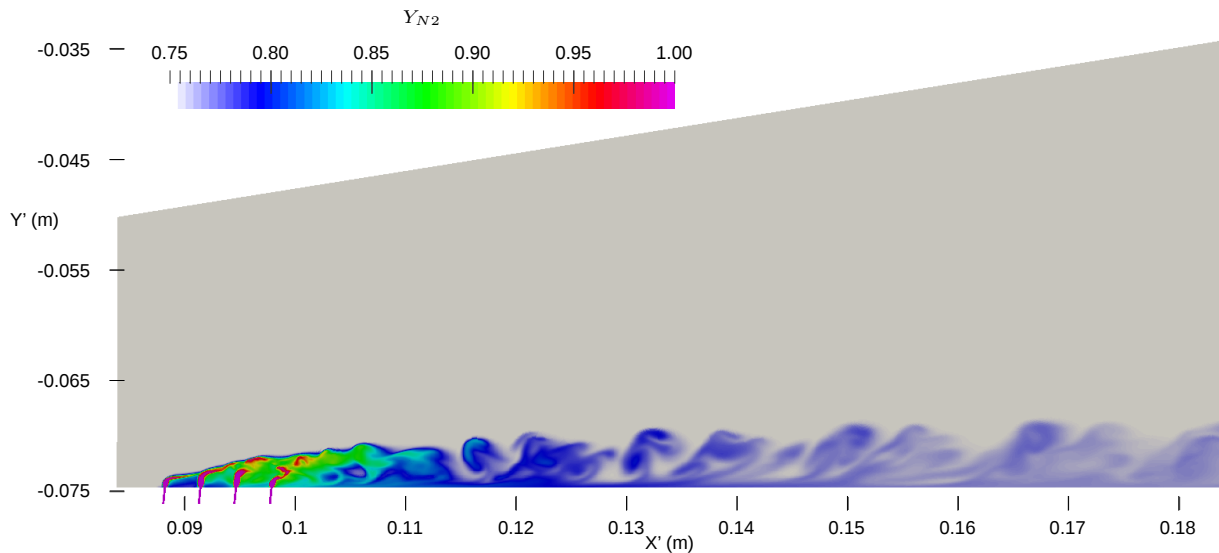

Fig 2. Nitrogen mass fraction Y_{N2}, symmetry plane colour map, $t = 7.0$

Figure 3 displays the temperature, showing additional flow features such as the leading edge shock and the incoming laminar boundary layer. Of interest is the size of the fuel plumes, which seem to be approximately matching the boundary layer in height. The boundary layer size to obstruction height ratio is an important parameter in studies of tripped transition, and has additional complexity in supersonic flow where the obstruction may be partially submerged in the subsonic region. The temperature map also seems to imply that the injection thickens the boundary layer somewhat, an observation that is borne out by more sophisticated analysis.
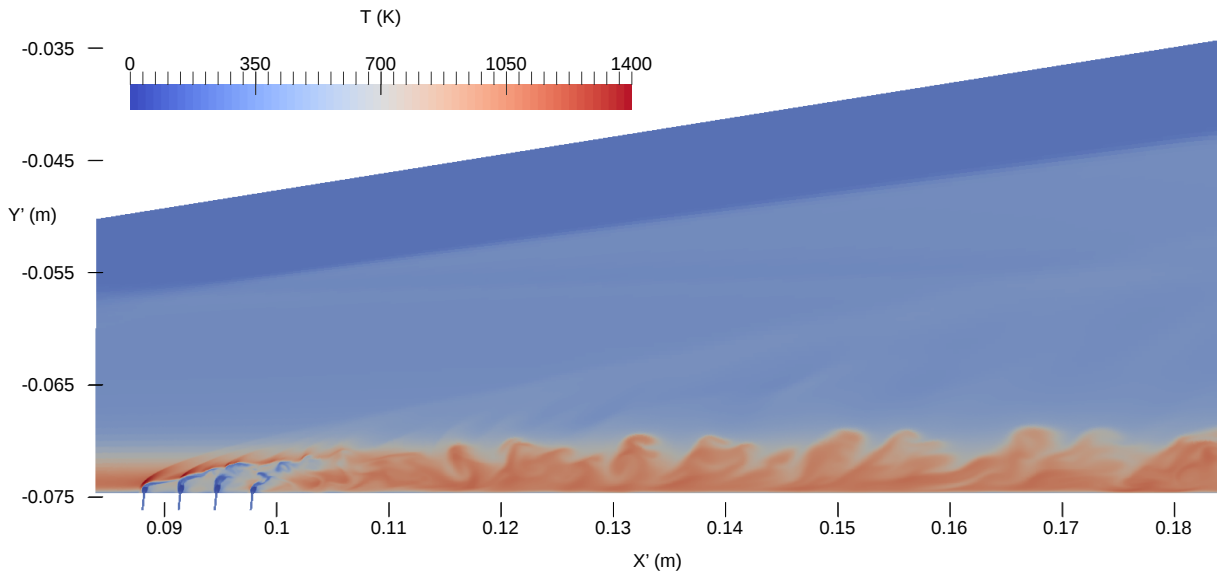
Fig 3. Temperature p (K), symmetry plane colour map, $t = 7.0$

Figure 4 displays the pressure field in a similar manner to the other figures. Though difficult to see in the image, animations of the flowfield show a curious phenomenon where the bow shock of the final injector in the array seems to be oscillating with a fairly well defined frequency, shedding waves into the downstream region that are visible in the plot as a series of striations or lines of high pressure. This phenomenon has important implications for the development of the turbulence further downstream, as boundary layer transition is known to be sensitive to certain frequencies. Optimally designed MPIA trips could target these frequencies to accelerate the process of transition, though it is presently unknown which parameters affect this phenomenon and how it might be controlled.
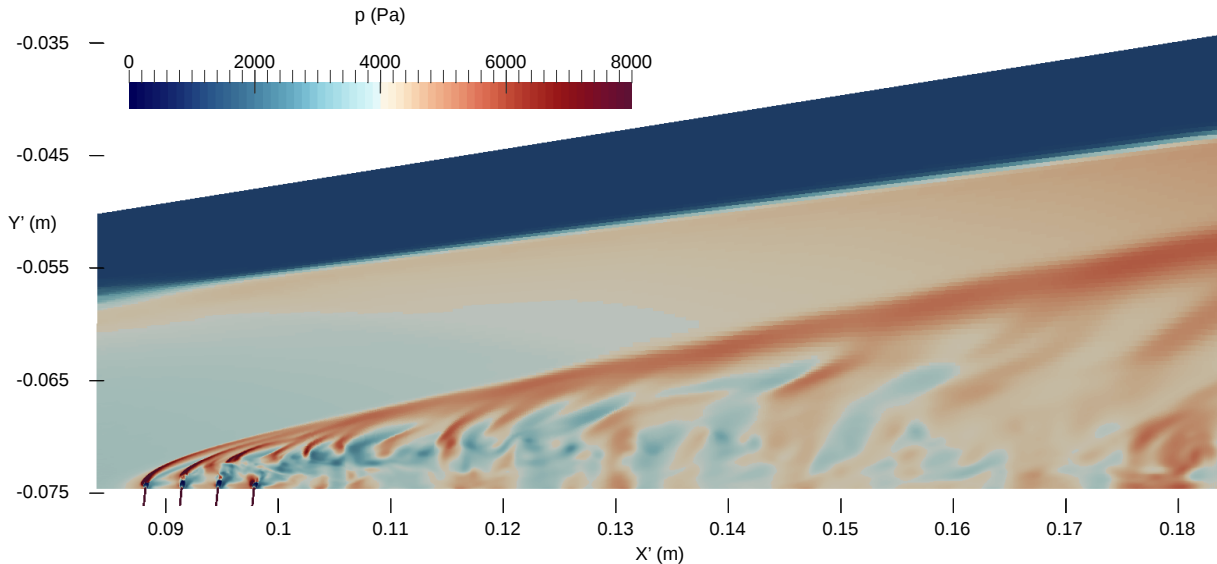

Fig 4. Pressure p (Pa), symmetry plane colour map, $t = 7.0$

5. Simulation Quality

5.1. LES Spatial Discretisation

The primary difficulty in performing an LES calculation is determining whether sufficient cell density is present to resolve the large eddies present in the turbulent region of the flow. Filtering the flow with too-large cells can cause erroneous results, since not enough momentum transport is being resolved by the turbulent fluctuations. In this work we assess the resolution of the LES by partitioning the turbulent kinetic energy into a resolved and modelled component, the former actually present in the simulation in the form of velocity fluctuations, and the latter computed from the subgrid IDDES model. A high quality LES calculation should have the majority of the energy in the resolved flow, and so their ratio can be used as a simulation quality metric, computed as follows.

The resolved flow energy is computed using the velocity fluctuations:

$$u_i' = \overline{u_i} - u_i \tag{11}$$

Where the bar $\overline{x}$ represents a time average, taken by averaging the velocity field over a sufficient number of timesteps. From this the resolved turbulent kinetic energy k_r can be calculated as:

$$k_r = \frac{1}{2} u_i' u_i' \tag{12}$$

The kinetic energy present in the modelled eddies k_m can be estimated using a result from [20], involving the kinematic turbulent viscosity ν_t, a constant derived from dimensional analysis $c_v^k = 0.07$, and the filter width Δ (estimated using the local cell size):

$$k_m = \frac{\nu_t^2}{(c_v^k \Delta)^2} \tag{13}$$

These components can be combined into a metric that expresses the fraction of resolved turbulent kinetic energy R. Values of above $\approx 80\%$ indicate that the LES model is being used in manner in which the models were intended, and implies that the calculation is well-resolved. Figure 5 plots this metric through the injector symmetry plane, using the time averaged k_r and k_m computed over 13 and 22 flowtimes respectively.

$$R = \frac{\overline{k_r}}{\overline{k_r} + \overline{k_m}} \tag{14}$$

The results indicate that the downstream and near jet region have high resolution, with 90% or more of the turbulent kinetic energy present in the resolved flow. These are the critical areas where the flow is transitioning from unsteady structured flow to turbulent-like irregular motion, and also where the injectant plumes begin to interact with the laminar fluid from the surrounding boundary layer. The only identified problem areas are surrounding the first and second jet plumes, where the initially laminar inflow reaches the MPIA and begins to transition. In these areas both k_r and k_m are low since the flow is non-turbulent, and the low R values are more indicative of a malfunction in the resolution metric than a problem with the grid. In light of these factors, the results of this section indicate that the LES grid is well-resolved.
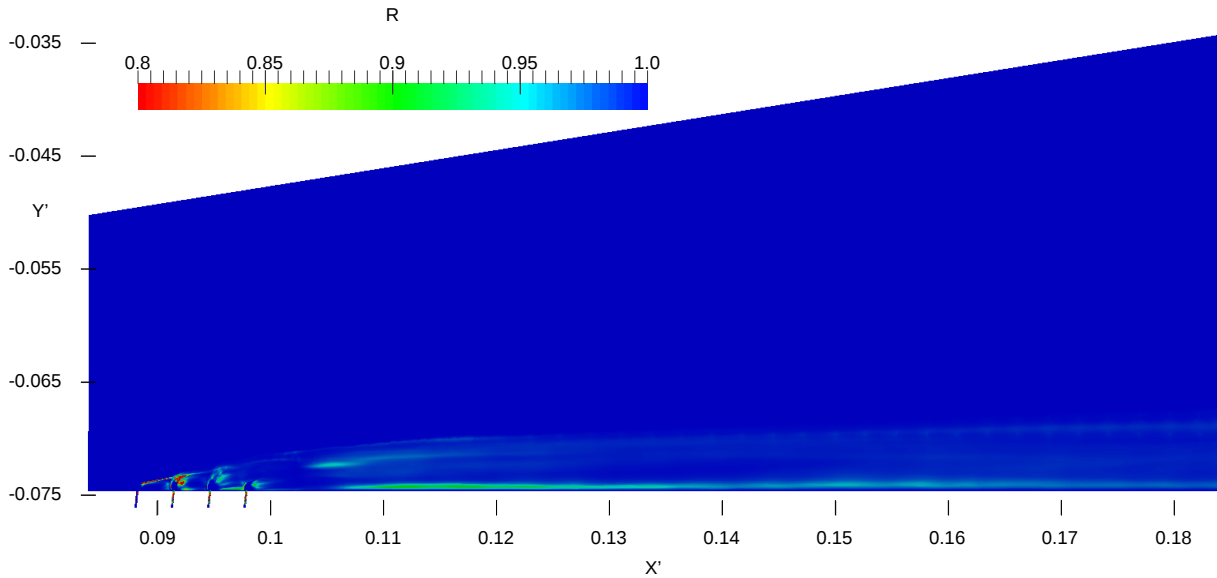
Fig 5. Resolved turbulent kinetic energy fraction R, symmetry plane colour map

5.2. LES Statistical Convergence

The time averages in equations 11 - 14 must be computed over a finite period of time that is long compared to the lowest frequency of the turbulent fluctuations. Figure 6 shows a time history of the simulation pressure at three points in the flow domain, each located just above the wall at $X' = 0.106, \ 0.152, \ 0.179$. Time is nondimensionalised using a flow time computed from the length of the domain ($\approx 0.1m$) and the post shock velocity ($\approx 2270m/s$): $t_f = 43.6\mu s$.

The simulation is divided into phases, marked by vertical dotted lines on the plots. Phase One displays the startup transients that appear in the flow as the turbulence develops from an initially steady state. Phases Two and Three correspond to the statistically stationary period where averages in time can meaningfully be computed. Most of the time averages ($\overline{u}_i$ for example) are computed over the entire phase 2 and phase 3 period, a total of approximately 14.5 flow times. Fluctuation quantities (such as $\overline{u'_i}$) which require a mean already converged are computed during phase three, assuming that their respective means are relatively well converged at the end of phase two.
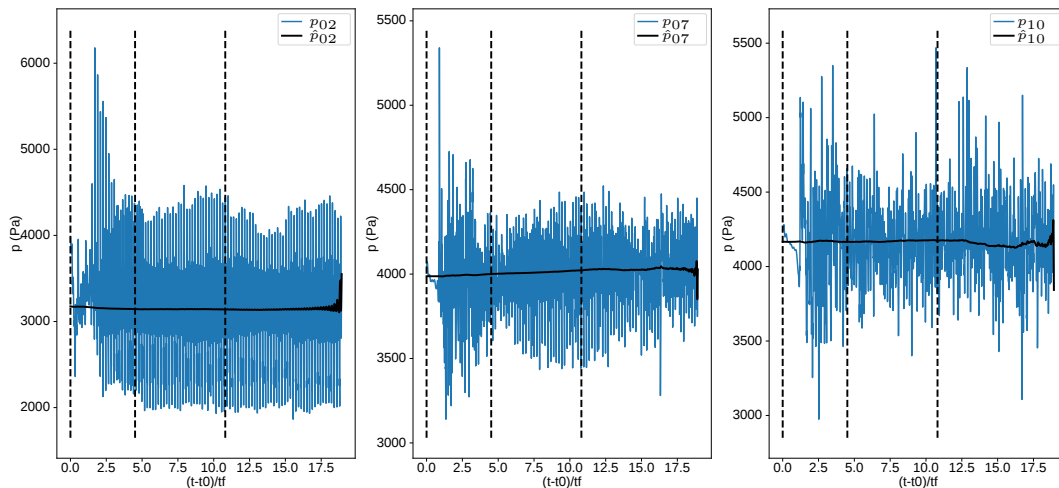

Fig 6. Pressure fluctuation history during LES phases of the simulation

Thus each phase should be approximately the size of the averaging window needed for converged statistics. The size of this window can be judged using the black line overlayed on each image, a reverse cumulative average $\hat{p}$ computed by starting at each time in the data set and averaging forward in time until the end. For a finite set of times between t_0 and t_1 the operation can be formalised as:

$$\hat{p}(t) = \int_{\tau=t}^{\tau=t_1} p(\tau)d\tau \qquad (15)$$

At the extreme right side the reverse average varies wildly due to the small number of points in the averaging window, but moving further to the left the line flattens out as the window becomes larger and more points are included. The amount of simulation time that it takes for the line to flatten out is then an indicator of the appropriate averaging window size. The actual data show that the fluctuations get more random and take longer to stabilise as the measuring point moves further downstream. This is to be expected given the turbulence is developing in space along the wall. However even in the most downstream case the averaging windows seem to be sufficient to have converged.

6. Transition Mechanics

6.1. Vortex Visualisation

A straightforward but informative analysis of the flow domain comes from plotting the vortex cores emanating from the injectors. Figure 7 shows such a figure, including pressure colour maps of the wall and periodic boundary conditions for illustrative purposes.
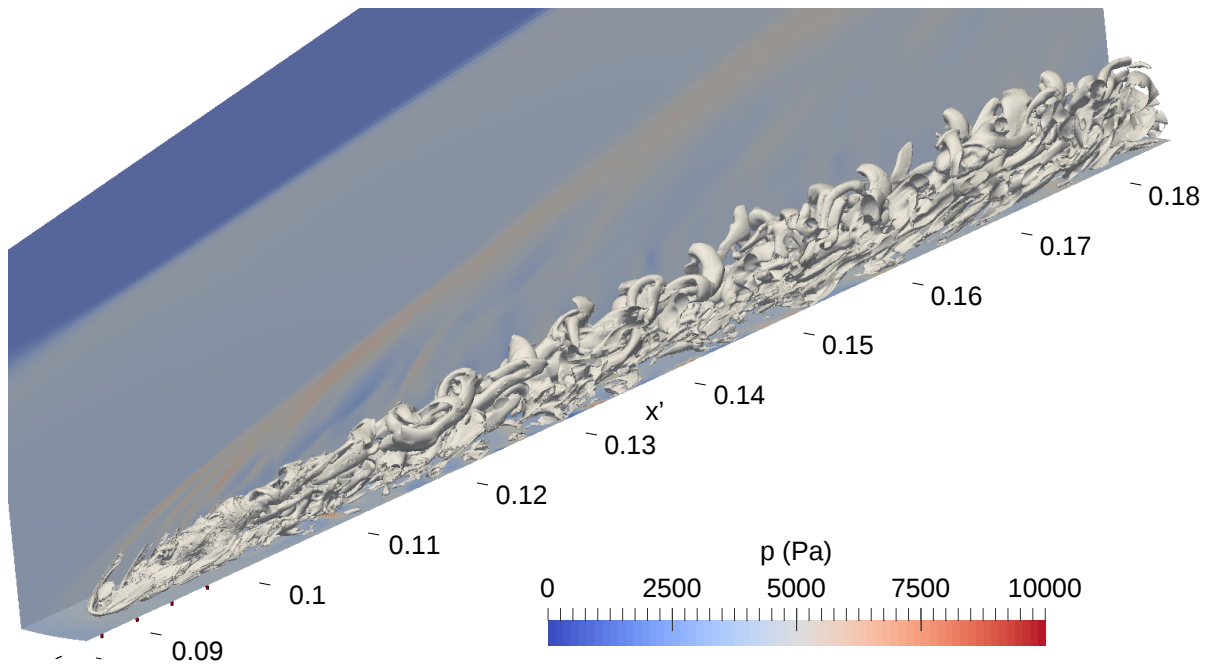

Fig 7. Vortex visualisation using TDM and the L2 method with pressure colour maps.

The vortices have been computed using the L2 decomposition, in which the velocity gradient is first decomposed into a symmetric strain tensor S_{ij} and an antisymmetric vorticity tensor W_{ij}. The two tensors are matrix-squared and then added to get a new matrix L. Areas of the flow where this matrix has two negative eigenvalues indicate local pressure minima, and thus can be used as indicators of where the vortex cores are.

$$S_{ij} = \frac{1}{2}\left[\frac{\partial u_i'}{\partial x_j} + \frac{\partial u_j'}{\partial x_i}\right] \qquad (16)$$

$$W_{ij} = \frac{1}{2} \left[\frac{\partial u_i'}{\partial x_j} - \frac{\partial u_j'}{\partial x_i} \right] \tag{17}$$

$$L_{ik} = S_{ij} S_{jk} + W_{ij} W_{jk} \quad : \quad eigvals(L) = \lambda_1, \lambda_2, \lambda_3 \tag{18}$$

To assist with visualisation, the dash velocity gradients $\partial u_i'/x_j$ in the above equations are not the ordinary velocity gradients, but have been processed using the Triple-Decomposition Method of [21]. This process subtracts out pure shearing from the velocity gradients, leaving only irrotational strain (S) and rigid body rotation (W). This is especially helpful in hypersonic flow for removing shockwaves and other non-vortex sources of shearing that would otherwise clutter the visualisation. (See [22] for more information.)

Figure 7 represents 3D contour surfaces where the second eigenvalue λ_2 is equal to -1×10^9. The visualisation clearly shows the size of the injectant plume as well as the increasing disorder as vortices develop downstream, a similar result to other Large Eddy Simulations of jets in supersonic cross-flow. In this case the similarity is significant only because of the size of the injectors. The MPIA injects directly into the boundary layer and a reasonable observer might doubt whether the plume could achieve sufficient penetration to develop into a turbulent state. The simulation clearly shows that it does.

6.2. Spectral Analysis

In this subsection we will use a Fourier transform to plot the spectral energy of the signals shown in figure 6, using the X-component of velocity records from phases 1 and 2. Although these signals represent time histories at a fixed point in space, they can be transformed into an effective spatial signal using the method of [23]. This procedure multiplies each instant of time in the signal record by the instantaneous magnitude of the velocity vector at that time, effectively creating a spatial record of the turbulence with uneven distributions between samples due to the fluctuations in velocity.

$$u(t_i) \mapsto u(s_i) \quad : \quad s_i = \sum_{j=0}^{i} \Delta t_j |\mathbf{u}_j| \tag{19}$$

For a set of N signals $u(s_n)$ the Discrete Fourier Transform is defined as:

$$U(k_i) = \sum_{n=0}^{N-1} u(s_n) e^{-i2\pi i n / N} \tag{20}$$

This operation produces a set of complex numbers representing the amplitude and phase of the waves making up the signals, which are useful for analysing the size and distribution of vortical structures present in the turbulence. Since evaluating this transform is expensive for large signals, a standard Fast Fourier Transform algorithm is used instead, though this adds the requirement that the signals be equally spaced in the real domain. Since the temporal to spatial mapping procedure used in equation 19 produces unevenly spaced points, a simple linear interpolation of $u(s_i)$ is used to remap the velocity signals onto a set of points separated by the constant value Δs, the mean of the separations of s_i.

The spectral energy of the resulting spectrum is then computed using:

$$E(k_i) = \left(\frac{|U(k_i)|}{N} \right)^2 \tag{21}$$

Additionally, rather than performing a single FFT of the entire signal history, the dataset is chopped into overlapping windows (eight windows of four flowtimes each), and the spectra computed for all the windows are averaged together. This reduces the amount of sampling noise in the signal and additionally
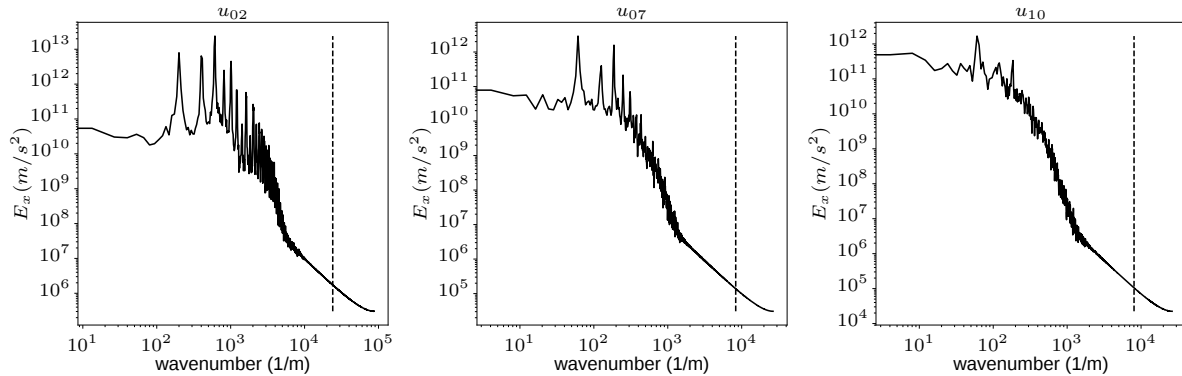
Fig 8. X-component velocity spectrum energy E_x for points 02, 07, and 10.

cuts off spurious high wavelength modes that would otherwise cause problems. The results for the three points sampled in the flow domain are shown in figure 8.

On the y axis the spectral energy of each wave is plotted (roughly speaking its magnitude in the decomposition), starting with large structures on the left (low wavenumber, high wavelength) and moving down toward smaller structures (high wavenumber, low wavelength) to the right. The dotted line represents the Nyquist wavenumber, computed from two cell lengths, the smallest possible structure resolvable on the numerical grid.

The most interesting feature of the computed spectra is the forest of sharp peaks present at high wavenumbers, particularly at point 02, which indicate a dominant frequency somewhere around $k = 2 \times 10^2 m^{-1}$ with several higher frequency harmonics. These are the periodic structures visible in the pressure colour maps, the result of rhythmic oscillations in the shock structure around the jet. Moving downstream to point 07 the dominant mode has lost some of its energy and most of the harmonics are no longer present, and by point 10 the dominant frequency is the only one remaining. This decay of initially ordered disturbances into a smooth blend of frequencies is a key feature of turbulent transition, but the spectra demonstrate that this process is only partially complete at the outflow to the domain.

At high wavenumbers all three spectra contain a strange feature: A clean section of constant slope with that begins well above the cutoff wavenumber and terminates just beyond it. This area of the spectrum seems to be dominated by red (or Brownian) noise, produced by random floating point rounding errors in the code being integrated in time. The telltale signs of red noise are a spectral density proportional to $1/f^2$, as well as the signature little foot at the largest wavenumbers where the source of the original (white) noise is present. This implies that small scale fluctuations in the CFD are being dispersed by the numerical scheme and flowing back up the spectrum until they meet the turbulent fluctuations flowing back down. The turbulent fluctuations, being much larger in magnitude, then dominate the upper part of the spectrum.

6.3. Wall Heat Transfer

This subsection compares results from the LES simulation to some preliminary experimental data, as well including two RANS models that are commonly used in the MPIA literature, with the goal of assessing their overall accuracy. Both turbulent transition and heat transfer prediction are notable challenges for CFD modelling, so the lessons of the analysis may have a more general application beyond MPIA flow dynamics specifically.

The wall heat transfer rate is computed as the dot product of the wall normal vector n_j and the heat conduction vector q_j (equation 10):

$$q = q_j n_j \tag{22}$$

Figure 9 displays the normalised non-dimensional heat transfer to the wall behind the MPIA. Heat transfer rates have first been nondimensionalised into Stanton numbers by dividing by the heat capacity of the freestream fluid:

$$St = \frac{q}{\rho_{\mathrm{inf}} u_{\mathrm{inf}} (h_0 - c_p T_w)} \tag{23}$$

Additionally, the nondimensional heat transfers have been normalised by the laminar heat transfer rate, as predicted by a laminar CFD solution with no MPIA injection (in the simulated results), and as measured by a laminar experimental test with no MPIA injection (in the experimental results). This normalisation cancels out any systematic bias in the sensors and focuses the analysis on the performance of the turbulence models in accounting for the difference. Thus the normalised heat transfer St/St_{lam} is shown in figure 9.
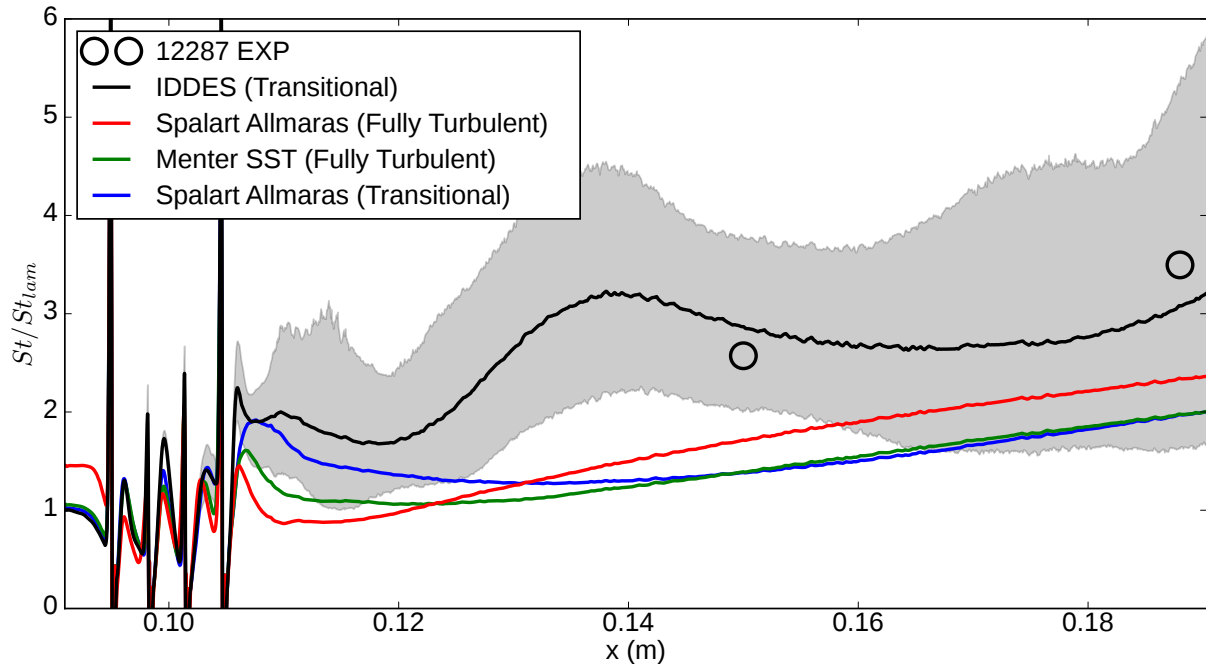

Fig 9. Normalised MPIA wall heat transfer, turbulence model comparison.

Figure 9 contains the results of four simulations. The first is the high fidelity LES calculation using the IDDES turbulence model. This simulation is marked "Transitional" to indicate that it uses a laminar inflow, computed from the larger, coarser simulation and fed into the fine grid using an inflow boundary condition. This is consistent with the experimental results, where the boundary layer is known to be laminar until the MPIA.

Also included are two RANS turbulence models that are popular in the hypersonics community, the one-equation Spalart-Allmaras (SA) model and the two equation Menter Shear-Stress-Transfer (SST) model. SST in particular has been used for a number of MPIA investigations such as [4] and [5]. These simulations use a slightly different inflow based on turbulent-from-the-leading-edge RANS with their respective models, and hence are marked "Fully Turbulent". The final simulation is an SA-RANS calculation initialised in the same manner as the LES, using a laminar inflow, and hence is marked "Transitional" in the same way.

The most obvious result from the figure is that in all the simulations the heat transfer behind the MPIA is higher than in the laminar flow, i.e. $St/St_{lam} > 1$. This indicates that any film cooling effect that may be present is cancelled out by the immediate transition to turbulence that occurs behind the final injector. The "fuel" in this cases is actually molecular Nitrogen (an inert substitute for the short hydrocarbons used in the other experiments), which is heavier than the Hydrogen typically used by MPIA researchers, lowering its potential for film cooling. Nonetheless the results are consistent with the hydrogen experiments of [8], who found no film cooling in the laminar/transitional case.

The next important difference is that the LES results predict higher heat transfer than any of the RANS results, which are cluster together lower down on the graph. The different methods also demonstrate qualitative differences. The RANS results are characterised by a slow, almost linear, rise in the region past the MPIA. In contrast the LES results display some interesting structure, a rapid rise to a local peak, and then an area of roughly flat mean heat transfer where the variance grows as the turbulence develops. These variances are indicated by the grey shaded area on the graph, representing the 5th and 95th percentile values of the unsteady heat transfer dataset used to compute the mean. Obviously this higher order information is unavailable for the RANS simulations, but it is interesting to inspect the size of the fluctuations in heat transfer, which do not simply vary around the mean but flow past the wall in huge spikes and troughs reach up to almost twice the mean in some places, and down almost to laminar level in others.

The final point of comparison is the experimental data points, outlined as black circles on the plot. The results imply that the RANS models are underpredicting the turbulent heat transfer, and that the LES model is predicting it reasonably well. There are not enough data points to check whether the qualitative trend in the LES simulation is right (a quick increase followed by a shallow rising trough), but the results are much closer to the mean of the LES results than the RANS calculations are, likely due to the LES model's greater sophistication in handling the complex flow physics involved.

7. Conclusions

A numerical investigation of a supersonic, non-reacting, Multiport Injector Array has been undertaken using high-fidelity Large Eddy Simulation. The simulated conditions matched an experimental setup where the MPIA is used to transition the boundary layer on a model scramjet inlet, at conditions matching Mach 7.6 with a dynamic pressure of 50kPa.

The simulated flow field consisted of an unsteady plume of injectant flowing out of the injectors and mixing turbulently with the boundary layer. The turbulent structures in this plume are highly three dimensional and not fully developed, without a clear separation between low wavenumber energy containing scales and high-wavenumber dissipative structures. Superimposed on the turbulent field are large scale harmonic disturbances in the ≈ 100 kHz range, generated by periodic oscillations of the shock structure around the MPIA. This behaviour seems to emerge from poorly understood coupling between the jets, where unsteady motion from an upstream jet excites forced oscillations in a downstream one, producing disturbances that pass into the boundary layer for many hundreds of millimetres. Since boundary layer transition is known to be sensitive to certain frequencies, it may be possible to tune this phenomenon to promote rapid transition behind an MPIA used specifically as a trip. At present however, not much is known about the relationship between these frequencies and MPIA variables such as injector radius, freestream momentum ratio, and spacing. Better analytical and LES/DNS modelling will be needed to establish this relationship.

A second important issue addressed in this paper is the fidelity of numerical turbulence models for predicting heat transfer in complex MPIA flowfields. A preliminary experimental comparison suggests that the real heat transfer behind the MPIA is quite high compared to the laminar level, due to turbulent transport of high momentum freestream flow down toward the wall. The RANS frameworks tested underpredicted this difference, starting with a low value close to the laminar level and rising slowly and smoothly in the streamwise direction. In contrast the LES results are fairly close to the experimental measurements and provide a much richer simulation of the physics of mixing and transition in the near wall region. This greater success is due to the resolved motion present in the LES solution; the ed-

dies, shocklets, hairpins, and vortices that transport momentum and energy in much the same way as the real turbulence does. Future numerical studies of MPIA behaviour that make specific claims about heat transfer levels or mixing performance should consider using unsteady turbulence modelling such as LES or DNS. These models may be complex, but this complexity is well-suited to the reality of the MPIA flowfield, and the results of high-fidelity modelling can be used to tune and validate lower-fidelity models, which in turn are applied to physical experiments in wind tunnels and flight models, and in turn to the development of a next generation of flying hypersonic aircraft.

Acknowledgements

References

[1] R. J. Goldstein, E. R. G. Eckert, F. K. Tsou, and A. Haji-Sheikh, "Film cooling with air and helium injection through a rearward-facing slot into a supersonic air flow," *AIAA Journal*, vol. 4, June 1966.

[2] R. J. Goldstein, E. R. G. Eckert, and D. J. Wilson, "Film cooling with normal injection into a supersonic flow," *Transactions of the ASME*, pp. 584–588, November 1968.

[3] A. S. Pudsey and R. R. Boyce, "Numerical investigation of transverse jets through multiport injector arrays in supersonic crossflow," *Journal of Propulsion and Power*, vol. 26, pp. 1225–1236, November-December 2010.

[4] A. S. Pudsey, R. R. Boyce, and V. Wheatley, "Hypersonic viscous drag reduction via multiporthole injector arrays," *Journal of Propulsion and Power*, vol. 29, pp. 1087–1096, September 2013.

[5] M. B. Gerdroodbary, M. Imani, and D. D. Ganji, "Investigation of film cooling on ose cone by a forward facing array of micro-jets in hypersonic flow," *International Communications in Heat and Mass Transfer*, vol. 64, pp. 42–49, 2015.

[6] A. Pudsey, V. Wheatley, and R. R. Boyce, "Supersonic boundary-layer combustion via multiporthole injector arrays," *AIAA Journal*, vol. 53, pp. 2890–2906, October 2015.

[7] R. J. Stalker, "Control of hypersonic turbulent skin friction by boundary-layer combustion of hydrogen," *Journal of Spacecraft and Rockets*, vol. 42, July 2005.

[8] K. Basore, M. Selzer, V. Wheatley, R. Boyce, D. Mee, B. Capra, M. Kuhn, and S. Brieschenk, "Performance comparison of distributed injectioni methods for hypersonic film-cooling," in *20th Australiasian Fluid Mechanics Conference*, (Perth, Australia), December 2016.

[9] W. O. Landsberg, N. N. Gibbons, V. Wheatley, M. K. Smart, and A. Veeraragavan, "Improving scramjet performance through flow field manipulation," *Journal of Propulsion and Power*, vol. 34, pp. 578–590, May-June 2018.

[10] G. V. Candler, H. B. Johnson, I. Nompelis, P. K. Subbareddy, T. W. Drayna, and V. Gidzak, "Development of the us3d code for advanced compressible and reacting flow simulations," in *53rd AIAA Aerospace Sciences Meeting*, no. 2015-1893, (Kissimmee, Florida), January 2015.

[11] M. Shur, P. Spalart, M. Strelets, and A. Travin, "A hybrid rans-les approach with delayed-des and wall modelled les capabilities," *International Journal of Heat and Fluid Flow*, vol. 29, pp. 1638–1649, 2008.

[12] S. R. Allmaras, F. T. Johnson, and P. Spalart, "Modifications and clarifications for the implementation of the spalart-allmaras turbulence model," in *Seventh International Conference on Computational Fluid Dynamics*, (Big Island, Hawaii), 9-13 July 2012.

[13] P. Subbreddy and G. Candler, "A fully discrete, kinetic energy consistent finite-volume scheme for compressible flows," *Journal of Computational Physics*, vol. 228, pp. 1347–1364, 2009.

[14] F. Ducros, V. Ferrand, F. Nicoud, C. Weber, D. Darracq, C. Gacherieu, and T. Poinsot, "Large-eddy simulation of the shock/turbulence interaction," *Journal of Computational Physics*, vol. 152, no. 2, pp. 517–549, 1999.

[15] I. Nompelis, T. W. Drayna, and G. V. Candler, "Development of a hybrid unstructured implicit solver for the simulation of reacting flows over complex geometries," in *34th AIAA Fluid Dynamics Conference*, no. 2004-2227, (Portland, Oregon), 28th June-1st July 2004.

[16] M. Wright, G. Candler, and M. Prampolini, "Data-parallel lower-upper relaxation method for the navier-stokes equations," *AIAA Journal*, vol. 34, pp. 1371–1377, July 1996.

[17] S. Gordon and B. J. McBride, "Computer program for calculation of complex chemical equilibrium compositions and applications," Tech. Rep. Reference Publication 1311, National Aeronautics and Space Agency, 1994.

[18] C. R. Wilke, "A viscosity equation for gas mixtures," *Journal of Chemical Physics*, vol. 18, pp. 517–519, April 1950.

[19] P. K. Subbareddy, M. D. Bartkowicz, and G. V. Candler, "Direct numerical simulation of high-speed transition due to an isolated roughness element," *Journal of Fluid Mechanics*, vol. 748, pp. 848–878, 2014.

[20] R. M. Gehre, *The Flow Physics of Inlet-Fueled, Low-Compression Scramjets*. PhD thesis, The University of Queensland, School of Mechanical and Mining Engineering, St Lucia, QLD 4072, 2014.

[21] V. Kolář, "Vortex identification: New requirements and limitations," *International Journal of Heat and Fluid Flow*, vol. 28, pp. 638–652, May 2007.

[22] N. Gibbons, R. Gehre, S. Brieschenk, and V. Wheatley, "Blast wave-induced mixing in a laser ignited hypersonic flow," *Journal of Fluids Engineering*, vol. 140, pp. 1–10, May 2018.

[23] P. Buchave and C. M. Velta, "Measurement of turbulent spatial structure and kinetic energy spectrum by exact temporal-to-spatial mapping," *Physics of Fluids*, vol. 29, 2017.